ELSEVIER

Contents lists available at ScienceDirect

Materials & Design

journal homepage: www.elsevier.com/locate/matdes





Influence of high-strain-rate compression and subsequent heat treatment on $(TiNbZr)_{89}(AlTa)_{11}$ refractory high-entropy alloys: Dynamic-mechanical behavior and microstructural changes

Muhammad Abubaker Khan ^a, Jamieson Brechtl ^b, Muhammad Hamza ^c, Chuangshi Feng ^d, Adil Mansoor ^e, Bushra Jabar ^{f,**}, Peter K. Liaw ^{g,*}, Mohamed A. Afifi ^{h,i,*}

- ^a Beijing Advanced Innovation Center for Materials Genome Engineering, School of Materials Science and Engineering, University of Science and Technology Beijing, Beijing 100083. China
- ^b Buildings and Transportation Science Division, Oak Ridge National Laboratory, Oak Ridge, TN 37830, USA
- ^c Institute of Advanced Materials, Bahauddin Zakariya University, Multan, Pakistan
- ^d Songshan Lake Materials Laboratory, Dongguan 523808, China
- ^e College of Physics and Optoelectronic Engineering, Shenzhen University, Shenzhen 518060, China
- f Institute for Metallic Materials, Leibniz Institute for Solid State and Materials Research Dresden, 01069 Dresden, Germany
- g Department of Materials Science and Engineering, University of Tennessee, Knoxville, TN 37996, USA
- ^h Mechanical Engineering Program, School of Engineering and Applied Sciences, Nile University, Giza 12677, Egypt
- ⁱ Smart Engineering Systems Research Centre (SESC), Nile University, Giza 12677, Egypt

ARTICLE INFO

Keywords: Refractory high-entropy alloy Dynamic mechanical properties Microstructural evolution

Strain-rate-sensitivity

ABSTRACT

This study explored the dynamic-mechanical behavior of a novel low-density (TiNbZr)₈₉(AlTa)₁₁ refractory highentropy alloy (RHEA) across strain rates ranging from 1.0×10^3 to 3.5×10^3 s⁻¹. A significant increase in the yield and ultimate compressive strengths with rising strain rates up to 3.0×10^3 s⁻¹ was observed and attributed to enhanced dislocation activities and stress-induced microstructural transformations. The formation of the B2 phase and Zr₅Al₃ precipitates was found to be crucial in bolstering the alloy strength at high strain rates. Beyond strain rates of 3.0×10^3 s⁻¹, a decrease in strength occurred due to thermal softening and strain localization. Microstructural analyses at 3.5×10^3 s⁻¹ revealed grain refinement, the development of micro shear bands, and dislocation tangles, which were indicative of dynamic recrystallization. Besides, the findings also revealed that the post-dynamic compression heat treatment further enhanced the hardness and microstructural stability of the alloy. These results highlight the potential of the (TiNbZr)₈₉(AlTa)₁₁ RHEA for applications requiring materials with high strength-to-weight ratios, particularly in dynamically loaded environments. It is expected that the results of this study will further advance our fundamental understanding of the behavior of RHEAs under extreme conditions, thereby opening new avenues for material innovation.

1. Introduction

A fundamentally important objective within the field of materials science is to resolve the inherent trade-off between the strength and ductility of advanced metallic materials. Typically, metallic materials are subject to strain-rate effects wherein the yield strength increases, and the ductility decreases with an increase in the strain rate [1]. Furthermore, as the strain rate rises, the influence of thermal activation on dislocations declines while the effect of viscous drag on dislocation

motion becomes more prominent [2]. Both factors would result in an increase in the Peierls-Nabarro stress [3], hence contributing to the overall strengthening of the material. During the process of dynamic deformation, the rapid multiplication of high-density dislocations impedes their ability to glide easily. As a result, a significant accumulation of dislocations occurs, leading to the concentration of stress and the propagation of cracks at the initial stage of deformation [4]. Furthermore, as the strain rate increases, both the shear stress and the adiabatic effect increase significantly, resulting in severe deformation localization

E-mail addresses: bushrajabbar_786@outlook.com (B. Jabar), pliaw@utk.edu (P.K. Liaw), mafifi@nu.edu.eg (M.A. Afifi).

https://doi.org/10.1016/j.matdes.2024.113062

^{*} Corresponding authors at: Mechanical Engineering Program, School of Engineering and Applied Sciences, Nile University, Giza 12677, Egypt (Mohamed A. Afifi).

^{**} Corresponding author.

and the generation of adiabatic shear bands (ASBs) [5]. Accordingly, the ductility of the material is impaired. Hence, the enduring problem in the field of metallic materials pertains to the trade-off between strength and ductility with increasing strain rate.

In recent years, researchers have introduced and created a new category of alloys known as high-entropy alloys (HEAs). These alloys are formed by combining multiple elements, typically four or more, in nearequiatomic proportions ranging from 5 to 35 atomic percent (at.%) [6]. The HEA strategy has effectively overcome these limits imposed by traditional alloy-design methods, such as limited base elements and complicated microstructures, resulting in a significant increase of alloydesign possibilities [7]. Through the manipulation of the composition, scientists possess the capability to modify the microstructures of HEAs in order to attain specific mechanical properties. For instance, Al [8], Mo [9], Ti [10], V [11], Zr [12], Ta [13], Nb [14], and Y [15] have been added to the Cantor alloy as solutes, resulting in a multi-phase structure, which enhanced the strength of the material. The hardening of the alloys by adding elements as solutes can be attributed to a combination of solid-solution strengthening, second-phase strengthening, and finegrain strengthening.

Findings from a host of studies have shown that HEAs demonstrate exceptional mechanical properties [16], including elevated strength, outstanding ductility [17], dynamic-impact strength [18,19], superior fracture toughness [20], and favorable thermal stability [21]. Until now, investigations [7,22] have predominantly concentrated on the distinctive mechanical behavior exhibited by different HEAs. However, the various mechanical responses of HEAs under severe conditions, such as high strain rates, have garnered growing interest within the domains of materials science and mechanics [23].

Among the existing HEA systems, face-centered-cubic (FCC)-based HEAs have been extensively studied under dynamic loading [24,25]. In the context of FCC-structured HEAs, it has been observed that the stacking-fault energy and the critical stress required for twinning are influenced by the intricate chemical environment at the individual level [26]. The occurrence of deformation twins serves to mitigate stress concentrations resulting from dislocation tangling and the accumulation of large numbers of dislocations [27]. Consequently, FCC HEAs often demonstrate an effective combination of elevated strength and adequate ductility under dynamic-loading conditions [28]. Though, the bodycentered-cubic (BCC) structure in RHEAs, which mainly contain refractory elements and exhibit considerable potential for dynamic applications [24,29], hinders twinning deformation due to their high stacking-fault-energy (SFE). It is crucial to note that in BCC materials, the concept of 'high SFE' indirectly reflects the complex energy barriers to deformation mechanisms like twinning, necessitating a deeper exploration beyond traditional FCC contexts [30].

Furthermore, the reduced thermal conductivity of RHEAs, which is a result of the inherent properties of their constituent atoms, might exacerbate the occurrence of adiabatic shear effects [31]. The reduced thermal conductivity of RHEAs, in turn, poses significant difficulties and complexities in achieving ductilization under dynamic-loading conditions. Hypothetically, the mitigation of severe deformation localization and the development of ASBs in RHEAs could potentially lead to an increase in their ductility under dynamic-loading conditions [5].

Accordingly, in the present research, room-temperature compression experiments were conducted on a newly designed (TiNbZr) $_{89}$ (AlTa) $_{11}$ RHEA subjected to dynamic-loading within the range of 1×10^3 – to 3.5×10^3 s $^{-1}$. An integral part of this investigation involves exploring the potential of post-dynamic compression heat treatment to optimize the mechanical properties of RHEAs. This approach aims not only to enhance our knowledge of the fundamental mechanisms influencing the balance between strength and ductility in these alloys, but also to develop novel alloy compositions and treatment protocols that can surmount current limitations in ductility while preserving high strength. Furthermore, the goal of the present research is to enhance microstructural properties through exposure to the high strain rates and

subsequent heat treatment, thereby contributing to the development of materials designed for performance in harsh environments. Therefore, it is believed that the current research is pivotal in the ongoing advancement of alloy design, offering novel insights and pathways for material innovation in sectors where good mechanical performance is critically demanded.

2. Material preparations

Ingots of the (TiNbZr)₈₉(AlTa)₁₁ (at. %) RHEA were produced using a vacuum-melting furnace. The constituent metals, sourced commercially, had a purity level exceeding 99.9 %. During arc melting, a mixture of these constituent elements was melted in an atmosphere consisting of argon gas. The specific operational procedure for melting involves the amalgamation of the alloy's source components within the crucible. The technique utilizes an arc current ranging from 60 to 70 A. When the arc is initiated, it is initially melted on a crucible holding pure Ti for a duration of 1–2 min. This step serves to eliminate the oxygen present in the furnace, hence preventing oxidation of the HEA during the melting process. Afterwards, the alloy is melted using a smelting current ranging from 200 to 300 A. The alloy samples underwent multiple cycles of melting, with a minimum of 10 repetitions, in order to achieve consistent melting and enhance their chemical uniformity. Following casting, a homogenization treatment was performed at 750 °C for 3 h and then at 1,050 °C for 4 h to achieve a consistent microstructure. The selection of these temperatures was guided by a combination of a series of optimization experiments, and the specific characteristics of the RHEA [32]. The density of the RHEA was estimated using the Archimedes method [33]. Additionally, the phase structure, microstructure, and chemical composition prior to compression were examined by X-ray diffraction, SEM (Apreo, Thermo Scientific, Netherlands), electron backscatter diffraction (EBSD), and an energy-dispersive X-ray spectrometer (EDS), and the results were reported in our previous work [34]. Cylindrical specimens, measuring 4 mm in diameter and 4 mm in length, were prepared for dynamic and quasi-static-compression tests. The quasistatic-compression tests were conducted at room temperature, with the results reported in our previous work [34]. Additionally, dynamiccompression tests with strain rates ranging from 1.0 \times 10³ to 3.5 \times 10³ s⁻¹ were carried out using a split Hopkinson pressure bar (SHPB). The compression tests were performed at least three times for reproducibility. The samples were fractured after compression at a strain rate of $3.5 \times 10^3 \text{ s}^{-1}$. Post-compression microstructure investigation was performed using EBSD techniques. Besides, after dynamic-compression tests, the strains were assessed employing kernel average misorientation (KEM) methods (by the Aztec software) [35]. Further, microstructures were investigated using a transmission electron microscope (TEM; Tecnai G2 F20) equipped with a selected area electron diffraction (SAED) system and operating at 200 kV. The TEM samples were prepared by electro-polishing, as described in previous studies [36]. The examination of the RHEA microstructure by TEM prior to compression is also reported in our previous work [34].

In the final phase of our experiments, the peak yield strength was achieved in the alloy after dynamic compression using a SHPB at a strain rate of $3.0 \times 10^3 \ s^{-1}$. Following this step, a solution treatment was applied to the samples at 1,000 °C for 30 min, succeeded by water quenching. Subsequently, the alloy underwent ageing at 600 °C for varying durations: 0 h, 2 h, 4 h, 8 h, 12 h, 16 h, 24 h, 48 h, and 72 h. This heat treatment aimed to determine the maximum hardness for microstructure analysis utilizing an ISO 6507-standard HV-1000Z micro-Vickers hardness tester at 10 kg-force loads for 15 s [37]. The hardness of the alloy was measured to assess the effect of the heat treatment. Twelve indentations were performed and spaced 0.5 cm in which the average hardness value was calculated.

M.A. Khan et al. Materials & Design 243 (2024) 113062

3. Results and discussion

The (TiNbZr)₈₉(AlTa)₁₁ RHEA demonstrates a very low density of 6.0 g/cm³, which is due to the notable presence of Ti (density of 4.5 g/ cm³) and Al (density of 2.7 g/cm³) [38,39]. Furthermore, the density of this RHEA is significantly lower than Inconel 718 (8.22 g/cm³), Mar-M247 (7.8 g/cm³), and most other RHEAs with densities exceeding 8.0 g/cm³, as reported in an earlier review article [5]. Given the significantly lower density of this RHEA compared to traditional hightemperature alloys, it becomes crucial to conduct mechanical testing at high strain rates to access its suitability for practical applications. Therefore, an examination is conducted on the dynamic-mechanical behavior and microstructural response of the recently developed lightweight RHEA employing mechanical testing at various strain rates. This analysis aims to evaluate the feasibility of using this material in practical applications, such as the mechanical components of automobiles as these components are often subjected to high strain rates due to collisions during driving.

3.1. Dynamic-mechanical properties

Fig. 1(a) displays the true stress-true strain curves of the (TiNbZ-r)₈₉(AlTa)₁₁ RHEA for strain rates ranging from 1.0×10^3 to 3.5×10^3 s $^{-1}$. The yield and ultimate compression strengths, as derived from the curves with standard deviations, are summarized in Table 1. It is apparent that the RHEA displays strain-rate sensitivity where strengths are increasing with increasing strain rates from 1.0×10^3 to 3.5×10^3 s $^{-1}$. For example, the dynamic-compressive yield strength and flow stress increase with increasing the strain rate up to 3.0×10^3 s $^{-1}$. The yield strength after compression at 3.0×10^3 s $^{-1}$ reaches a yield strength of 1,450 MPa. The yield strength of the HEA increases by 25 % after compression at 3.0×10^3 s $^{-1}$ by comparison with the HEA after compression at 1.0×10^3 s $^{-1}$.

The increase in strength may be due to interactions between the moving dislocations and phonons, which are defined as elastic vibrations within a crystal lattice or discrete quanta of vibrational mechanical energy [40]. Under strain rates higher than $10^3~{\rm s}^{-1}$, dislocations encounter a uniform distribution of phonons emanating from the surrounding area, their motion can be impeded due to a viscous drag effect caused by the phonons [41]. Moreover, these swift dislocations create localized temperature changes, leading to an irreversible heat flow and energy depletion in the dislocation, thereby reducing its mobility leading to locking of dislocations and increase in strength. Such a viscousdrag effect on the dislocations causes the solid to behave similarly to a Newtonian viscous material during dynamic deformation. The friction force applied to the dislocation by drag effects under dynamic conditions can be expressed as [2]:

Table 1 The yield and ultimate strengths of the RHEA tested at strain rates ranging from 1.0×10^3 to 3.5×10^3 s⁻¹.

Strain rate (S ⁻¹)	Yield strength (MPa)	Ultimate compression strength (MPa)
1.0×10^{3}	940 ± 12	$1,\!402\pm10$
1.6×10^3	$1,\!276\pm 8$	$1,\!437\pm 6$
2.1×10^3	$1,\!095\pm10$	$\textbf{1,445} \pm \textbf{8}$
2.5×10^3	$1{,}106\pm10$	$1,\!466\pm 5$
3.0×10^3	$\textbf{1,454} \pm \textbf{5}$	1,487 \pm 5
3.2×10^3	$1,\!329\pm 8$	1,485 \pm 8
3.5×10^3	$\textbf{1,254} \pm \textbf{6}$	$1,\!441\pm10$

$$f_{\nu} = B\nu = b\tau \tag{1}$$

where f_v is the friction force, B is the viscous coefficient, v is the dislocation velocity, τ is the shear stress, and b is the Burgers vector. The factor, B, is dependent on the dislocation velocity as follows [2]:

$$B = B_0 / \left(1 - \frac{v^2}{C_s}\right) \tag{2}$$

where B_0 is the viscosity at rest, and C_s is the shear-wave speed of materials. Thus, based on Eqs. (1) and (2), the dynamic-dislocation motions lead to a strong high strain-rate dependence of the flow stress [42]. Under high strain rates, the process of dislocation slip in metals is influenced by viscous damping, which includes both phonon and electron-drag viscosities. Studies have demonstrated [41,43] that particularly at room temperature, the phonon-drag viscosity is a significant factor in the damping process. Phonons, which are thermoelastic waves moving through the metal lattice, increase in intensity when the lattice is compressed. This intensification of thermal vibrations among the atoms leads to a corresponding increase in the viscosity associated with the phonon drag. The modified Z-A model considering the effect of phonon drag can be expressed as follows [41]:

$$Y = \sigma_o \exp(-\beta_o T + \beta_1 T \ln \varepsilon) \left(1 - \frac{\zeta \varepsilon}{\beta_1 Y}\right)^{-\beta_1 T} + \sigma_g$$
 (3)

where σ_o is the thermal stress at 0 K, β_o and β_1 are material parameters, ζ is a material parameter related to viscosity, Y is the initial yield strength, T is the temperature, ε is the strain-rate, and σ_g is the grain-boundary strengthening stress. This equation is important as it provides a relationship between the initial yield strength and factors, such as the temperature, strain rate, and grain-boundary strengthening stress.

Increasing the compressive strain rate to 3.2×10^3 and 3.5×10^3 s⁻¹ leads to a drop in the yield strength by 6 %. The drop in the yield strength can be attributed to thermal softening and strain localization [36,44]. Fig. 1(b) illustrates that the current RHEA exhibits an optimal

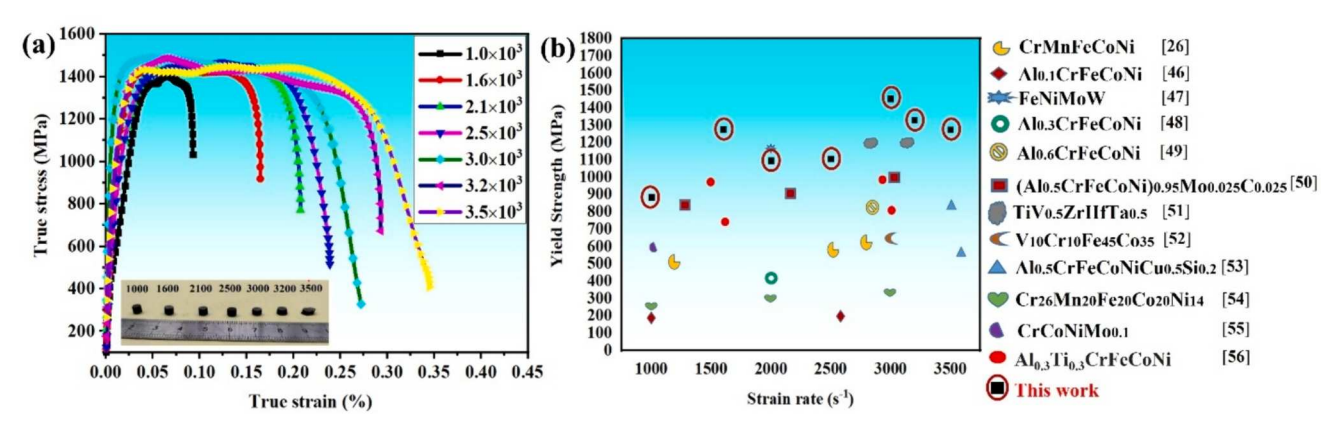


Fig. 1. (a) True stress–strain curves of RHEA deformed at strain rates ranging from 1.0×10^3 s⁻¹ to 3.5×10^3 s⁻¹, (b) comparison of the yield-strength values (MPa) of the current study against documented values found in the literature [23,45–55].

yield strength under high compressive strain rates, indicating its potential suitability for applications that involve exposure to such conditions. The second-phase particles, which consist of mainly of nano B2 and AlZr rich particles, are dispersed throughout the grains such that they hinder dislocation motion. These phases are homogeneously distributed and were detected on the as-cast RHEA, as presented in our previous study [34].

3.2. Post-dynamic-compression heat treatment

Fig. 2 presents the hardness profile of the RHEA after undergoing the post-dynamic compression heat treatment. According to the hardness chart, the peak hardness of approximately 870 HV was observed after ageing at 600 $^{\circ}\text{C}$ for 16 h. Consequently, to gain deeper insights into the effects of the heat treatment, the microstructure of the alloy, post-dynamic compression, and post-heat treatment at 600 $^{\circ}\text{C}$ for 16 h, was further examined using both SEM and TEM.

3.3. Microstructure characterization after dynamic testing

Typical EBSD-orientation maps of the (TiNbZr)89(AlTa)11 RHEA after compression at strain rates of $3.0 \times 10^3 \, \text{s}^{-1}$ and $3.5 \times 10^3 \, \text{s}^{-1}$ are shown in Fig. 3. These maps were recorded on the transverse sections perpendicular to the compression direction, Fig. 3(a) reveals that the RHEA compressed at $3.0 \times 10^3 \, \text{s}^{-1}$ had mostly equiaxed grains and a few fine small grains with average sizes of $\sim 50 \mu m$ (Fig. S1), which were significantly smaller than those found in the as-cast sample (193 μ m) investigated in our recent study [34]. Fig. 3(b) shows the sample after compression at a strain rate of $3.5 \times 10^3 \, \text{s}^{-1}$, which indicates the presence of equiaxed grains similar to that observed in Fig. 3(a), although they had a smaller average grain size of 24 µm (see Fig. S1). The dominant orientation texture was along {101} with the presence of $\{001\}$ and $\{111\}$ after compression at $3.0 \times 10^3 \text{ s}^{-1}$. The dominant orientation owes to the recrystallization that occurred during deformation. It was found that after compression at 3.5×10^3 s⁻¹, the dominant orientation was still along {001}.

The kernel average misorientation (KAM) of the alloy after compression at strain rates of $3.0 \times 10^3 \, \text{s}^{-1}$ and $3.5 \times 10^3 \, \text{s}^{-1}$ are presented in Fig. 3(c)–(d), respectively. The color gradient, ranging from blue to green, indicates the degree of angular misorientation between neighboring grains. Here, blue signifies areas of low misorientation that

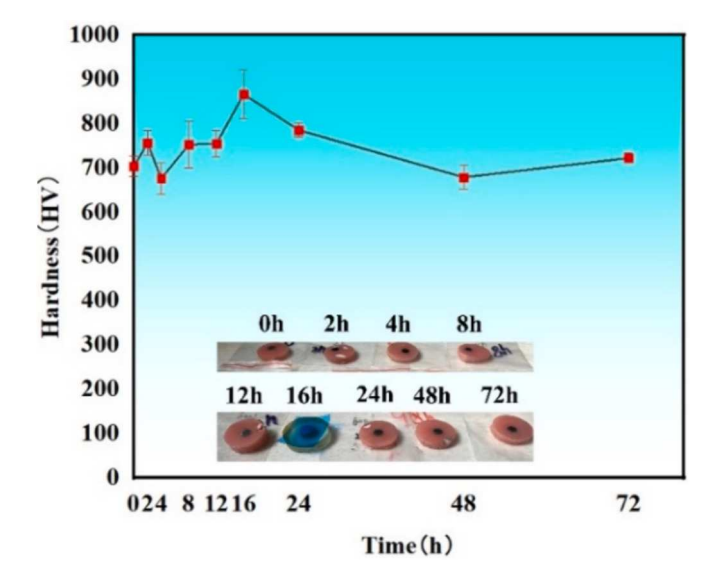


Fig. 2. Vickers micro hardness of the $(TiNbZr)_{89}(AlTa)_{11}$ RHEA after high-strain-rate compression and further ageing treatment at 600 °C for 0 h, 2 h, 4 h, 8 h, 12 h, 16 h, 24 h, 48 h, and 72 h.

is typical of uniform grain structures, while green to yellow hues represent higher misorientation that correspond to regions of internal strain or grain-boundary distortion. In contrast, Fig. 3(c) shows a higher degree of localized orientation. However, as depicted in Fig. 3(d), an increase in strain rate leads to a decrease in the localized orientation, which can be attributed to thermal softening [5]. The regions highlighted with arrows correspond to areas with high internal strains caused by the presence of micro shear bands. It is suggested that shear bands were only found at a very large, imposed shear strain. The work imposed upon the material during deformation can be used to calculate a (adiabatic) temperature rise inside the shear band using the following equation [2]:

$$dT = \frac{0.9}{\rho C_p} \tau d\gamma \tag{4}$$

where $\rho = 6.0 \,\mathrm{g/cm^3}$ is the density, τ is the shear stress, and C_D is the specific heat capacity. By using a weight averaging method, $C_p =$ $\omega_i \sum_{i=1}^5 C_{pi}(\omega_i)$ is the weight percent, and C_{pi} is the specific heat capacity for each element of the alloy) [56]. An increasing strain rate raises the imposed shear strain and leads to thermal heating and further fracture after high strain-rate compression. The presence of thermal heating and high-strain-rate compression leads to dynamic recrystallization and recovery after compression, leading to the grain refinement that is not present in the as-cast RHEA [34]. Fig. 3(c) features a large-strain area in the KAM map whereas for Fig. 3(a), fine grains can be observed within these large-strain regions in addition to very fine grains within the region suggested to be shear bands. It is important to clarify that shear bands are a particular kind of strain localization that involves strong shear deformation whereas strain localization is a broader term that includes any form of localized deformation in a material. Similar structures have been recently reported in α-Ti and identified as kink bands [57]. Increasing the strain-rate compression to 3.5×10^3 s⁻¹ results in thermal softening that leads to dynamic recovery and slight grain growth accompanied by reduced local strains, as confirmed through Fig. 3 (b) and (d).

Typical TEM micrographs of the RHEA subjected to high-strain-rate compression at $3.0 \times 10^3 \, \text{s}^{-1}$ and $3.5 \times 10^3 \, \text{s}^{-1}$ are displayed in Fig. 4 (a)-(b) and Fig. 4(c)-(d), respectively. Inspection of the bright-field (BF) micrograph in Fig. 4(a) reveals the presence of micro shear bands at different orientations in which these bands have great dislocation tangles. Weak beam-dark field (WBDF) TEM micrographs are displayed in Fig. 4(b), which features dislocations that are primarily entangled or in loops (white contrast within the shear band). Further analysis shows that the dislocations inside the shear bands consist mainly of screw dislocations with a g vector = [011] BCC, which is selected such that $|\hat{g} A \cdot bp| = 1$ where bp is a Burgers vector. Fig. 4(c) indicates that the shear bands with dislocation tangles are located within the shear bands, which is confirmed by the WBDF TEM image presented in Fig. 4(d). In this case, small dislocation loops and entanglements are heterogeneously distributed. However, as shown in Fig. 4(b), these features decreased with an increase in the strain rate. As mentioned earlier, this reduction is influenced by thermal heating and leads to fracture following high-strain-rate compression at $3.5 \times 10^3 \text{ s}^{-1}$. In the early phases of straining, high densities of dislocations emerge and reorganize into cellular substructures as strain increases. This process results in the subdivision of the original grains into smaller areas with significant misorientation [58]. The boundaries around these small areas consist of stored dislocations, which transform into finer grains with further straining [58,59].

High-magnification TEM images are displayed in Fig. 5. Fine, homogeneous precipitates can be observed in Fig. 5(a). These precipitates predominantly consist of the B2 and AlZr-rich phases, as confirmed by the SAED pattern along the $\langle 1\,1\,2\rangle$ BCC direction. Fig. 5(b) illustrates the presence of very fine precipitates along the grain boundaries. Following high strain-rate compression at 3.0×10^3 s⁻¹, the average size of these

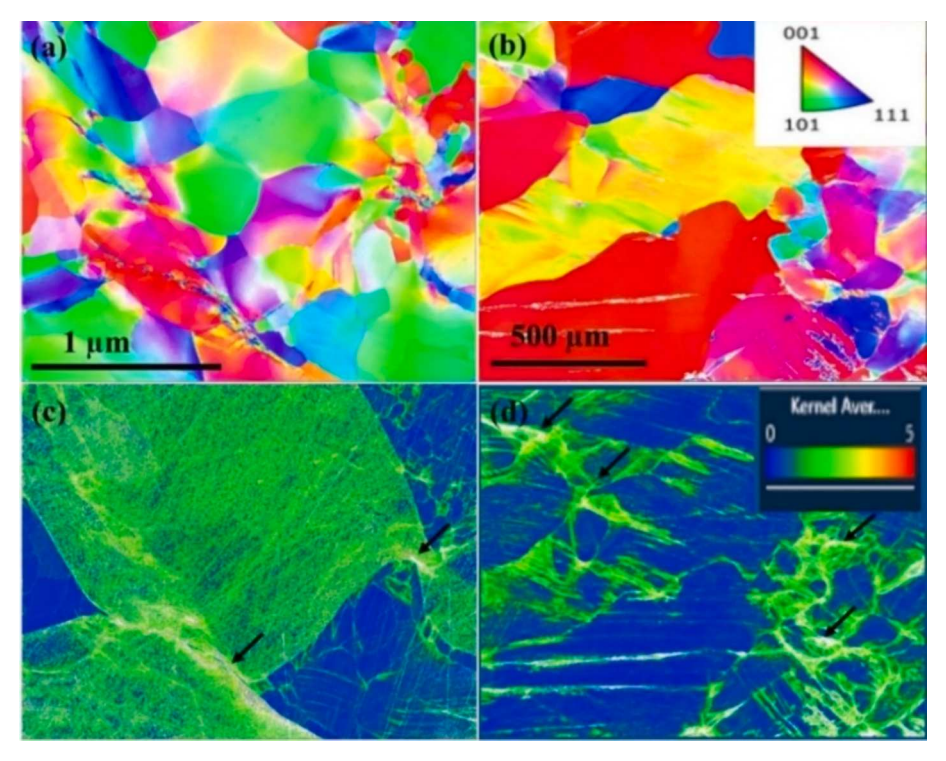


Fig. 3. (a), (b) EBSD orientation-color maps of the RHEA after compression at 3.0×10^3 s⁻¹ and 3.5×10^3 s⁻¹ and (c), and (d) KAM maps of the RHEA after compression at 3.0×10^3 s⁻¹ and 3.5×10^3 s⁻¹, respectively. Black arrows inserted in Fig. 3(c), and (d) correspond to the areas with large KAM referring to a high internal strain.

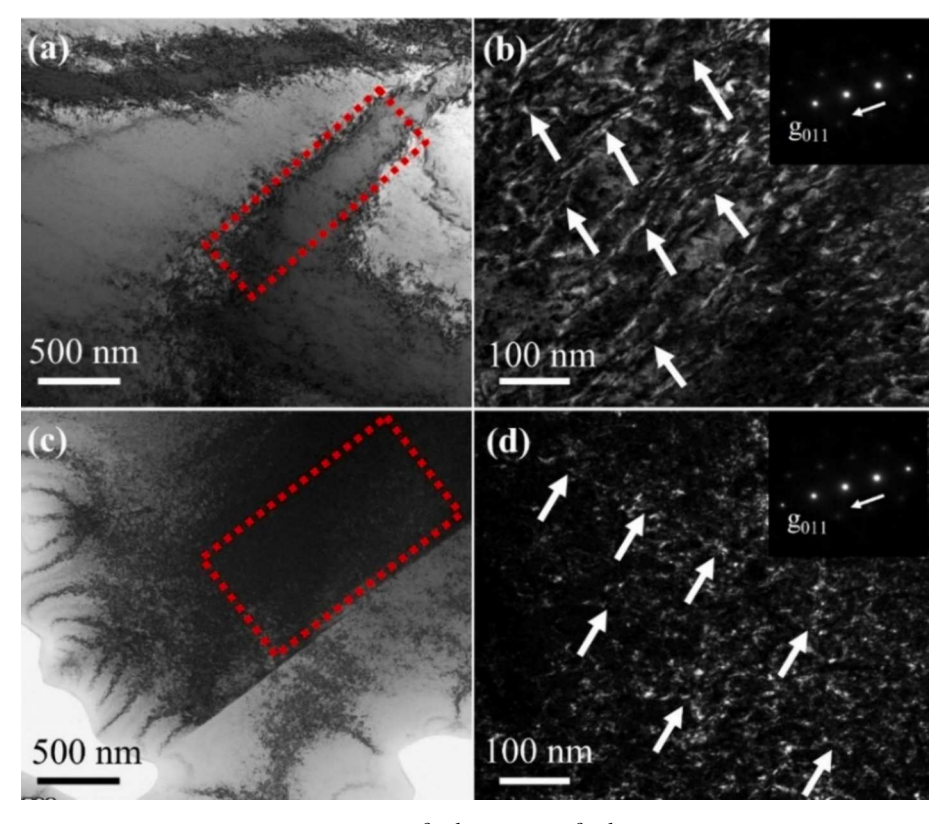


Fig. 4. Typical TEM micrographs of the RHEA after compression at 3.0×10^3 s⁻¹ and 3.5×10^3 s⁻¹ where (a-c) BF-TEM showing micro shear bands (indicated by the red-highlighted rectangle) and (b-d) WBDF-TEM indicating dislocation tangles (denoted by white arrows). Arrows inserted in the SAED images stand for the g-vector direction.

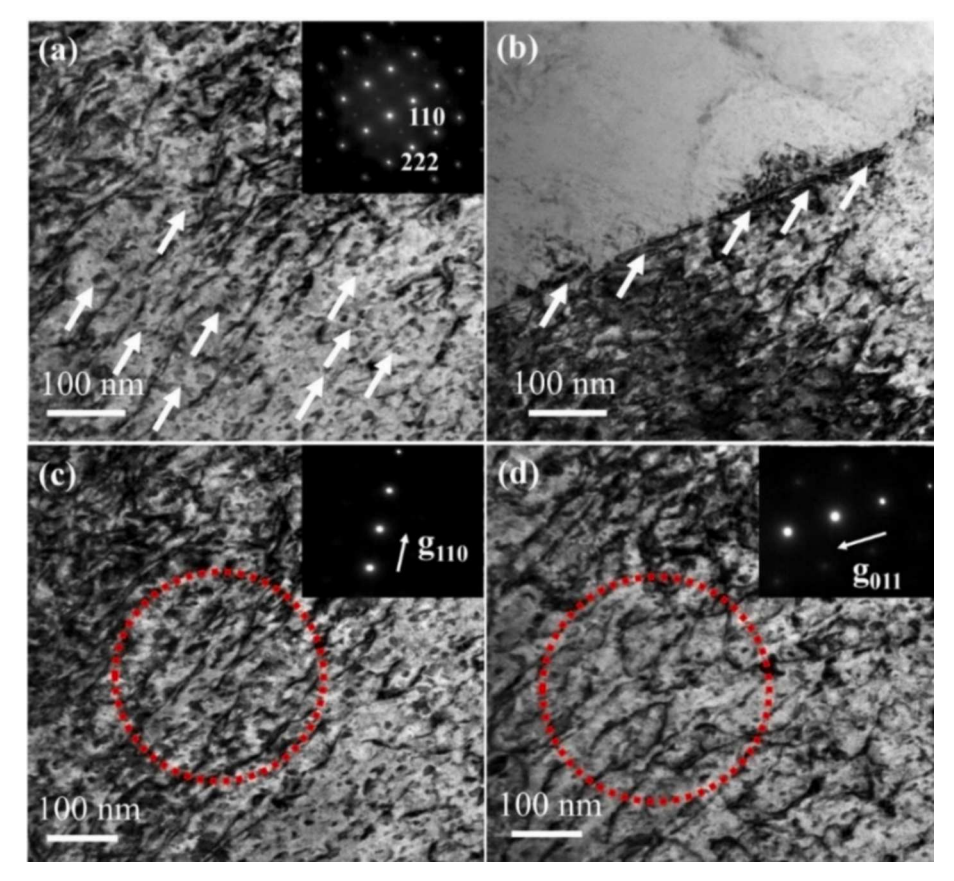


Fig. 5. The high-magnification BF-TEM images of the RHEA after high-strain-rate compression at $3.0 \times 10^3 \, \mathrm{s}^{-1}$ showing (a) a homogeneous distribution of fine precipitates, (b) fine precipitates along the grain boundaries (indicated by white arrows), Two-beam BF-TEM images of dislocations (indicated by red circles) in the deformed alloy imaged at the [111] $_{BCC}$ zone axis with (c) a g vector along [110] $_{BCC}$, and (d) a g vector along [011] $_{BCC}$. Arrows inserted in (Figs. c and d) the SAED images stand for the g-vector direction.

precipitate is ~ 20 nm, which is a 40 % reduction compared to those in the HEA before compression. This reduction is caused by dislocation shear occurring during the high strain-rate compression. Fig. 5(c) and 5 (d) show BF-TEM under the two-beam-condition images of dislocation networks after compression. Inspection of the two images indicates that some dislocations disappeared under a g vector, $[1\,1\,0]_{BCC}$, by comparison with dislocations observed under a g vector, $[0\,1\,1]_{BCC}$. It is suggested that the disappeared dislocations on the g vector of $[1\,1\,0]_{BCC}$ is screw dislocations where the g vector is perpendicular to the dislocation lines and/or edge dislocations, g, where the g vector parallel to the

dislocation lines [60,61]. This feature shows the evidence of a mixed type of dislocations observed after high-strain-rate compression. Furthermore, sessile dislocations, constituted by two 60° full dislocations, are detected along the g vector, $[011]_{BCC}$, as indicated by the arrow in Fig. 5(d).

 ${\it 3.4. \,\, Microstructure\, characterization\,\, after\, post-dynamic\,\, compression\, heat\,\, treatment}$

 $\begin{tabular}{ll} Fig. 6 shows EBSD images of the RHEA after dynamic compression at \\ \end{tabular}$

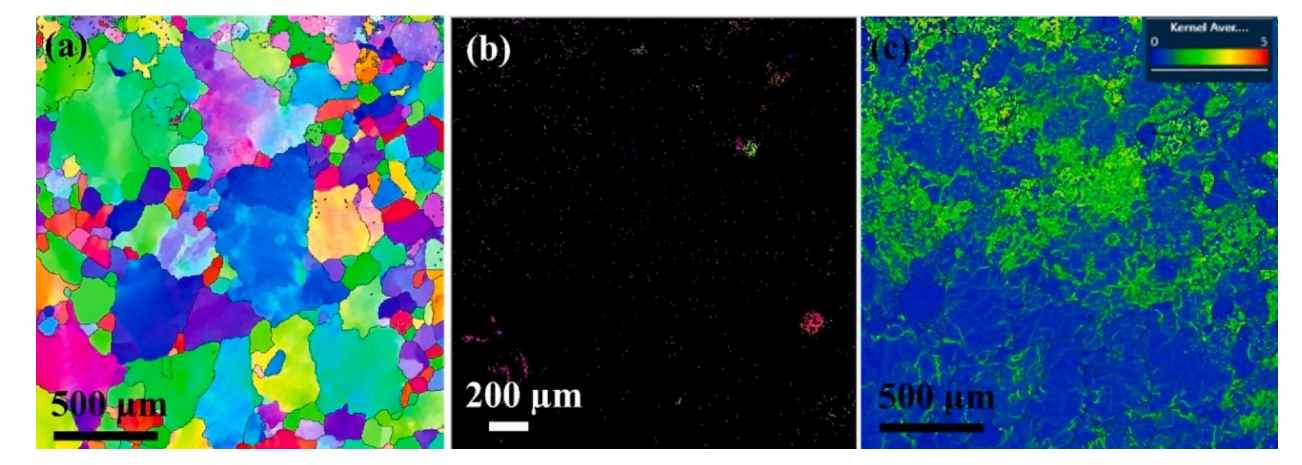


Fig. 6. EBSD micrograph of the RHEA after dynamic compression at 3.0×10^3 s⁻¹ followed by the peak- aging heat treatment showing (a) the grain structure (b) second-phase particles map (the coloured regions correspond to the particles) and (c) corresponding KAM map.

 $3.0 \times 10^3~s^{-1}$ and subsequent peak aging treatment at 600 °C for 16 h. Fig. 6(a) displays equiaxed grains where the average grain size in the HEA increased to 130 µm after high-strain-rate compression. Fig. S2 shows the grain-size distribution of the RHEA after dynamic compression at $3.0 \times 10^3~s^{-1}$, followed by the peak-aging treatment at 600 °C for 16 h. The phase map in Fig. 6(b) reveals the presence of agglomerated coarse second-phase particles that are heterogeneously distributed. Fig. 6(c) displays the results of the KAM analysis, which indicates that heat treatment led to a reduction in the internal strains of the sample by comparison with the sample before the heat treatment, as depicted in Fig. 3(c). Furthermore, the micro shear bands (denoted by the white arrows in the figure) became markedly smaller after the heat treatment [62].

The TEM micrographs shown in Fig. 7 illustrate the microstructural changes in the RHEA following the peak-aged heat treatment. Specifically, Fig. 7(a) highlights the existence of large, coarse particles intertwined with networks of dislocations, known as dislocation tangles. Conversely, Fig. 7(b) shows plate-like and spherical second-phase particles located within and along grain boundaries, where the volume fraction of precipitates is slightly higher (an average size of 20 nm) after the heat treatment. Furthermore, the insets of Fig. 7(b)-(c) feature a SAED pattern along $\langle 1\,1\,0\rangle_{BCC}$ indicates that B2 and Zr₅Al₃ phases [34,63] were present in the sample. Further inspection of the SAED pattern in Fig. 7(c) confirms the presence of the B2 phase adjacent to the grain boundaries along $\langle 110 \rangle_{BCC}$, which are coarse particles formed after the heat treatment. The WBDF-TEM image shown in Fig. 7(d) reveals a significant volume of fine second-phase particles that serve as pinning sites for dislocations, chosen with a g vector of [011] BCC to ensure $|g \cdot bp| = 1$, which are visible in white contrast where the dislocations are identified.

Fig. 8 exhibits an EDS map of the RHEA after dynamic compression at $3.0\times10^3~\text{s}^{-1}$ and subsequent peak-ageing heat treatment, which shows precipitates along a grain boundary. Fig. 8(a)–(b) show, respectively, BF-TEM and high-angle annular dark-field scanning-TEM (HAADF-STEM) micrographs of the grain-boundary precipitates. Fig. 8 (c) displays the solute variation of these precipitates, as determined by the EDS mapping. It was found that the precipitates predominately consisted of Al_3Zr_5 . Also, another group of precipitates was detected that contained a percentage of Ta and Nb, suggesting that they were B2 second-phase particles.

From these results, it is hypothesized that during aging, the equilibrium segregation of solutes to grain boundaries hastens the precipitation process, as compared to the bulk material. This hypothesis is substantiated by the presence of coarse particles observed along the grain boundaries after the aging treatment, as evidenced in Fig. 7(c) and 8(c). The presence of even a minimal quantity of this segregated impurity can significantly change both the microscopic dynamics of the defects and the overall behavior of the material [64,65]. The solute segregation isotherms based on the Langmuir adsorption, which was adopted for grain-boundary segregation by McLean [66], is given by:

$$(X_G B^1)/(1 - X_G B^1) = X_1/(1 - X_1) exp\left(-\frac{\Delta E_1}{RT}\right)$$
 (5)

where X_{GB}^1 is the atomic concentration of the solute I at the grain boundary, X_1 is the atomic concentration of the solute, I, in the matrix, E_1 is the internal energy of segregation of a solute atom, T is the temperature, and R is the universal gas constant. Based on Eq. (5), the solute segregation along grain boundaries is increasing with the peak-aged heat treatment, suggesting faster kinetics along the grain boundaries

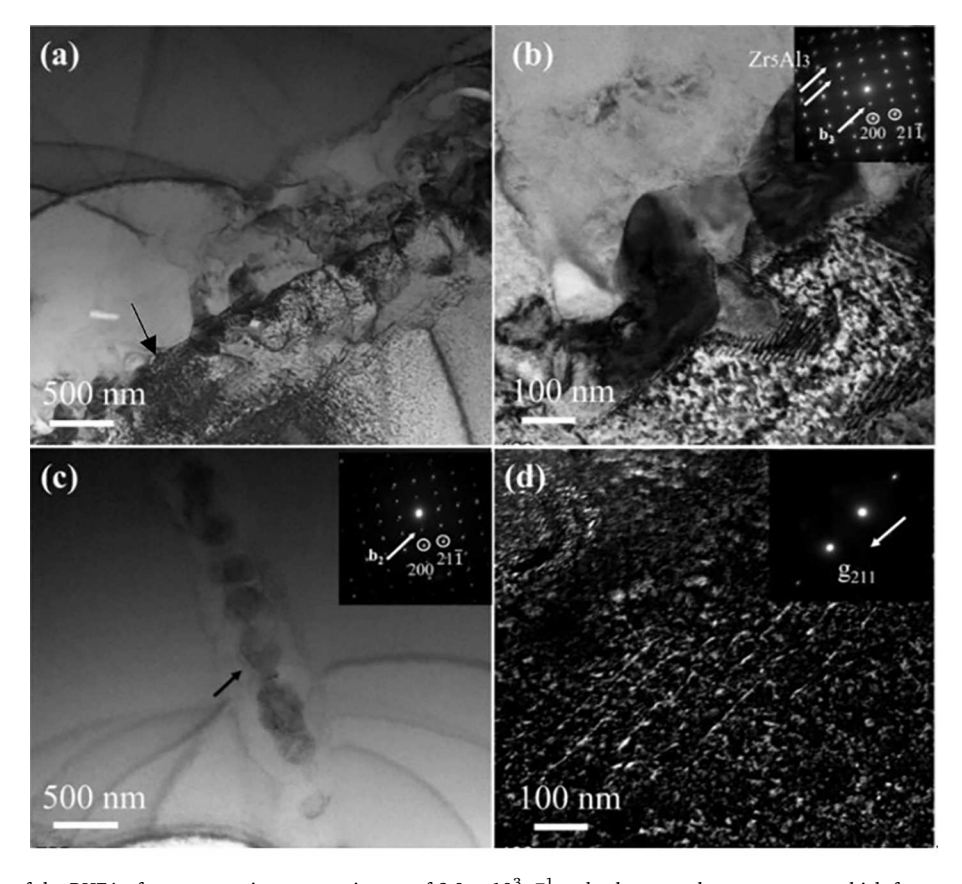


Fig. 7. TEM micrographs of the RHEA after compression at a strain rate of 3.0×10^3 s⁻¹ and subsequent heat treatment, which features (a) dislocation tangles as highlighted by black arrows, (b) second-phase particles with a corresponding SAED pattern, (c) grain-boundary second-phase particles, as highlighted by black arrows and (d) WBDF-TEM showing an array of dislocations with fine second-phase particles. Note: the white arrows inserted in the SAED patterns of Figs. (b)–(d) correspond to the g-vector direction.

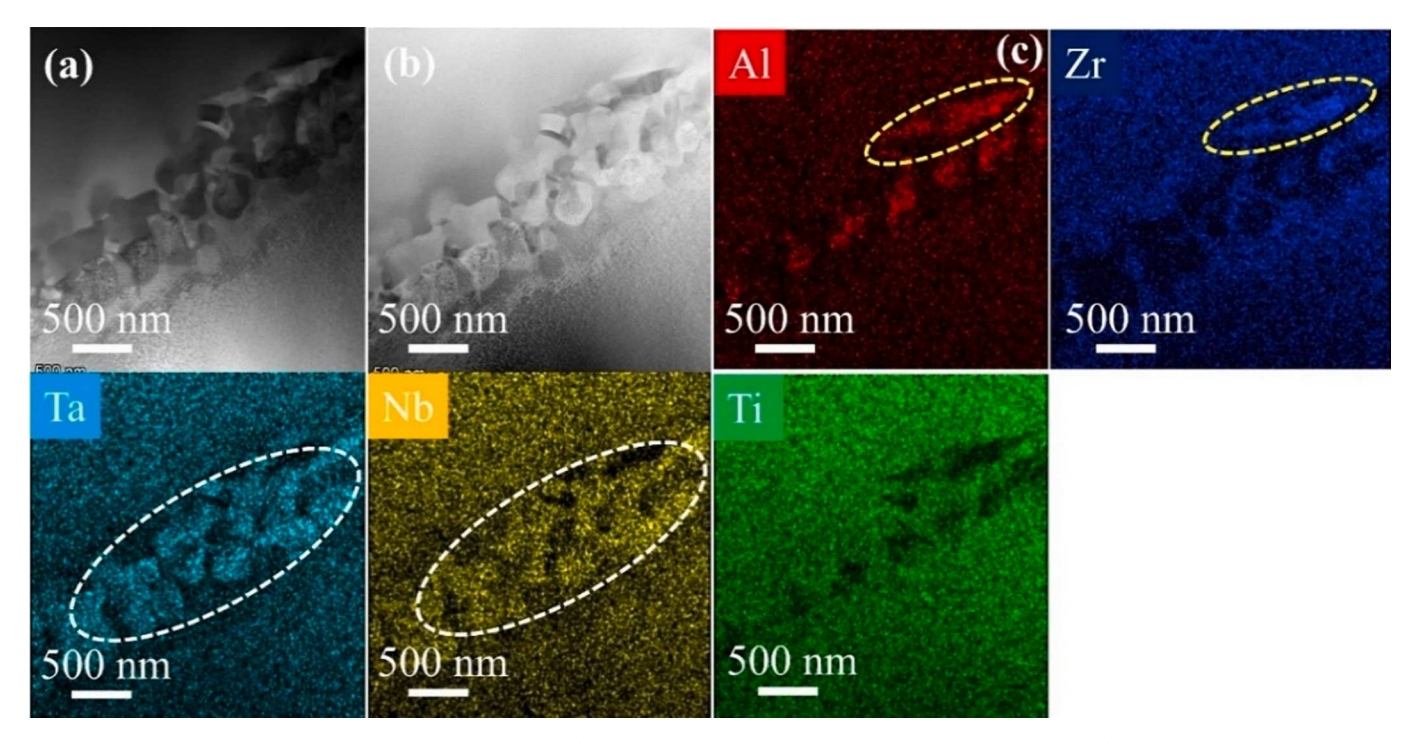


Fig. 8. (a) BF-TEM and (b) HAADF-STEM of second-phase particles along the grain boundary and (c) EDS mapping showing the presence of Al_3Zr_5 (contained a percentage of Ta and Nb, as indicated by the yellow ellipses) and B2 particles (contained a percentage of Ta and Nb, as indicated by the white ellipses).

by comparison with the interior grains. Such a scenario supports the increase in the number of second-phase particles. This result was confirmed by a recent finding, which provides direct evidence of the importance of entropy in grain-boundary segregation [67].

As previously stated, subjecting the samples to dynamic compression at a strain rate of 3.0 \times $10^3 \ s^{-1}$ resulted in the acceleration of agehardening processes within them. This finding was confirmed through hardness measurements conducted after the samples were subjected to heat treatment at 600 °C for 16 h. The peak hardness (Fig. 1) can be attributed to the fine precipitates coupled with dislocations, as observed in Fig. 6(b) and 7(b). It is proposed that the solute atoms (Ti, Nb, Zr, Al, and Ta) at substitutional sites cause lattice distortion, which can be mitigated to some extent when these atoms cluster around line defects and form what is known as a Cottrell atmosphere [68]. In this alloy, larger solute atoms tend to gather in the expanded areas of dislocations, especially near the dislocation core beneath the dislocation line. In contrast, smaller solute atoms are more likely to move to the compressed areas above the slip plane. Such migration leads to a concentration of solute atoms along the dislocation lines, forming solute-rich areas [69]. This movement towards the dislocation can occur through two primary mechanisms. First, the stress field generated by the dislocations can facilitate the migration of solute atoms. Second, the formation of Cottrell atmospheres is temperature-dependent: the temperature must be sufficiently high to enable defect migration, but not so high that it causes the atmosphere to disperse back into the solution matrix due to the impact of entropy on the free energy [70]. During the solution treatment, solutes tend to accumulate along dislocations. Subsequently, during the aging treatment, these solutes evolve into precipitates. Notably, after the heat treatment at 600 °C for 16 h, a multitude of fine, nanosized precipitates are formed. This result is clearly illustrated in Fig. 7(e), where these particles are homogeneously distributed within the grains. In summary, given their unique properties and the ongoing advancements in our understanding and production capabilities, HEAs hold promise in revolutionizing the performance and durability of mechanical components in the automotive industry.

4. Conclusions

The present research shows a comprehensive analysis of the $(TiNbZr)_{89}(AlTa)_{11}$ RHEA, demonstrating its unique dynamic-deformation behavior and offering insights into its microstructural evolution under various strain rates. The key findings are described as follows:

- 1. The $(TiNbZr)_{89}(AlTa)_{11}$ RHEA exhibits pronounced strain-rate sensitivity, with notable increases in the yield and ultimate compression strengths at strain rates up to $3.0 \times 10^3 \ s^{-1}$. This enhancement in mechanical properties is attributed to the intrinsic resistance of the material to deformation and the effective activation of dislocation mechanisms. Besides, the formation of the B2 phase and Zr_5Al_3 precipitates was found to be crucial in boosting the alloy strengths at high strain rates. However, at strain rates beyond $3.0 \times 10^3 \ s^{-1}$, a decline in yield strength is observed, likely due to thermal-softening and strain-localization phenomena. This behavior underscores the complex response of the alloy to dynamic stress, providing valuable insights for applications where variable strain rates are encountered.
- 2. Under dynamic compression, the RHEA undergoes significant microstructural changes, including grain refinement, formation of micro shear bands, and development of dislocation tangles. These transformations are indicative of dynamic recrystallization and recovery processes, which play a pivotal role in enhancing the strength and ductility of the material. The observed microstructural adaptability is crucial for the application of this alloy in environments subjected to extreme dynamic stresses.
- 3. The application of the post-dynamic compression heat treatment, particularly aging at 600 °C for 16 h, further refines the microstructure of the RHEA. This treatment leads to the development of second-phase particles and an increase in hardness, contributing significantly to the overall mechanical properties of the material. The effectiveness of this post-deformation heat treatment suggests a promising approach for tailoring the microstructure and enhancing the performance of RHEAs in practical applications.

- 4. The findings of this study highlight the potential of the (TiNbZ-r)₈₉(AlTa)₁₁ RHEA as a lightweight yet ultra-strong material suitable for dynamic applications.
- 5. The ability of the RHEA to maintain desirable strength-to-weight ratios, coupled with its adaptability under different strain rates and better properties after heat treatment, make it a promising material for engineering applications requiring durability and performance under dynamic stresses.

CRediT authorship contribution statement

Muhammad Abubaker Khan: Writing – review & editing, Writing – original draft, Investigation, Conceptualization. Jamieson Brechtl: Writing – review & editing, Validation. Muhammad Hamza: Writing – review & editing. Chuangshi Feng: Investigation. Adil Mansoor: Writing – review & editing. Bushra Jabar: Writing – review & editing, Validation, Conceptualization. Peter K. Liaw: Writing – review & editing, Supervision, Resources. Mohamed A. Afifi: Writing – review & editing, Writing – original draft, Validation, Investigation.

Declaration of competing interest

The authors declare that they have no known competing financial interests or personal relationships that could have appeared to influence the work reported in this paper.

Data availability

Data will be made available on request.

Acknowledgments

Muhammad Abubaker Khan would like to acknowledge the technical support from the Beijing Advanced Innovation Center for Materials Genome Engineering, School of Materials Science and Engineering, University of Science and Technology, Beijing, China. PKL very much appreciates the support from (1) the National Science Foundation (DMR – 1611180, 1809640, and 2226508) and (2) the Army Research Office (W911NF-13–1-0438, W911NF-19–2-0049, and FA9550-23-1-0503).

Appendix A. Supplementary data

Supplementary data to this article can be found online at https://doi.org/10.1016/j.matdes.2024.113062.

References

- [1] Z. He, N. Jia, H. Wang, et al., The effect of strain rate on mechanical properties and microstructure of a metastable FeMnCoCr high entropy alloy, Mater. Sci. Eng. A 776 (2020) 138982.
- [2] M.A. Meyers, Dynamic behavior of materials, John Wiley & Sons, 1994.
- [3] L. Zhang, Y. Xiang, J. Han, D.J. Srolovitz, The effect of randomness on the strength of high-entropy alloys, Acta Mater. 166 (2019) 424–434.
- [4] E. Ghassemali, R. Sonkusare, K. Biswas, N.P. Gurao, In-situ study of crack initiation and propagation in a dual phase AlCoCrFeNi high entropy alloy, J. Alloy. Compd. 710 (2017) 539–546.
- [5] O.N. Senkov, D.B. Miracle, K.J. Chaput, J.-P. Couzinie, Development and exploration of refractory high entropy alloys—A review, J. Mater. Res. 33 (19) (2018) 3092–3128.
- [6] J.W. Yeh, S.K. Chen, S.J. Lin, et al., Nanostructured high-entropy alloys with multiple principal elements: novel alloy design concepts and outcomes, Adv. Eng. Mater. 6 (5) (2004) 299–303.
- [7] W. Li, D. Xie, D. Li, et al., Mechanical behavior of high-entropy alloys, Prog. Mater Sci. 118 (2021) 100777.
- [8] J. He, W. Liu, H. Wang, et al., Effects of Al addition on structural evolution and tensile properties of the FeCoNiCrMn high-entropy alloy system, Acta Mater. 62 (2014) 105–113.
- [9] T.-T. Shun, L.-Y. Chang, M.-H. Shiu, Microstructure and mechanical properties of multiprincipal component CoCrFeNiMox alloys, Mater. Charact. 70 (2012) 63–67.
- [10] J. Wang, B. Zhang, Y. Yu, et al., Study of high temperature friction and wear performance of (CoCrFeMnNi)85Ti15 high-entropy alloy coating prepared by plasma cladding, Surf. Coat. Technol. 384 (2020) 125337.

[11] G.A. Salishchev, M.A. Tikhonovsky, D.G. Shaysultanov, et al., Effect of Mn and V on structure and mechanical properties of high-entropy alloys based on CoCrFeNi system, J. Alloy. Compd. 591 (2014) 11–21.

- [12] W. Huo, H. Zhou, F. Fang, et al., Microstructure and mechanical properties of CoCrFeNiZrx eutectic high-entropy alloys, Mater. Des. 134 (2017) 226–233.
- [13] H. Jiang, K. Han, D. Qiao, et al., Effects of Ta addition on the microstructures and mechanical properties of CoCrFeNi high entropy alloy, Mater. Chem. Phys. 210 (2018) 43–48.
- [14] X. Wen, Y. Wu, H. Huang, et al., Effects of Nb on deformation-induced transformation and mechanical properties of HfNbxTa0. 2TiZr high entropy alloys, Mater. Sci. Eng. A 805 (2021) 140798.
- [15] G. Polat, M. Tekin, H. Kotan, Role of yttrium addition and annealing temperature on thermal stability and hardness of nanocrystalline CoCrFeNi high entropy alloy, Intermetallics 146 (2022) 107589.
- [16] J.W. Choi, J.T. Kim, S.H. Hong, et al., Investigation of correlation between the microstructural characteristics and mechanical properties of (CoCuFeNi) 100-xAlx high entropy alloys, J. Alloy. Compd. 933 (2023) 167679.
- [17] C. Zhang, H. Wang, X. Wang, et al., Strong and ductile refractory high-entropy alloys with super formability, Acta Mater. 245 (2023) 118602.
- [18] J. Cheng, H. Qin, C. Li, et al., Deformation and damage of equiatomic CoCrFeNi high-entropy alloy under plate impact loading, Mater. Sci. Eng. A 862 (2023) 144432.
- [19] K. Cui, J. Qiao, P.K. Liaw, Y. Zhang, Data driving design of high-entropy alloys for lightweight and dynamic applications, Sci. China Phys., Mech. Astronomy 67 (2) (2024) 227101.
- [20] X. Liu, S. Zhang, H. Feng, et al., Outstanding fracture toughness combines gigapascal yield strength in an N-doped heterostructured medium-entropy alloy, Acta Mater. 255 (2023) 119079.
- [21] M. Wang, Y. Lu, J. Lan, et al., Lightweight, ultrastrong and high thermal-stable eutectic high-entropy alloys for elevated-temperature applications, Acta Mater. 248 (2023) 118806.
- [22] Q. Chao, J. Joseph, M. Annasamy, et al., AlxCoCrFeNi high entropy alloys from metal scrap: Microstructure and mechanical properties, J. Alloy. Compd. 976 (2024) 173002.
- [23] B. Wang, A. Fu, X. Huang, et al., Mechanical properties and microstructure of the CoCrFeMnNi high entropy alloy under high strain rate compression, J. Mater. Eng. Perform. 25 (2016) 2985–2992.
- [24] Y. Qiao, Y. Chen, F.-H. Cao, et al., Dynamic behavior of CrMnFeCoNi high-entropy alloy in impact tension, Int. J. Impact Eng. 158 (2021) 104008.
- [25] T. Zhang, S. Ma, D. Zhao, et al., Simultaneous enhancement of strength and ductility in a NiCoCrFe high-entropy alloy upon dynamic tension: Micromechanism and constitutive modeling, Int. J. Plast. 124 (2020) 226–246.
- [26] R.E. Kubilay, W.A. Curtin, Theory of twin strengthening in fcc high entropy alloys, Acta Mater. 216 (2021) 117119.
- [27] E.P. George, W.A. Curtin, C.C. Tasan, High entropy alloys: A focused review of mechanical properties and deformation mechanisms, Acta Mater. 188 (2020) 435–474.
- [28] D. Foley, S. Huang, E. Anber, et al., Simultaneous twinning and microband formation under dynamic compression in a high entropy alloy with a complex energetic landscape, Acta Mater. 200 (2020) 1–11.
- [29] M. Abubaker Khan, T.-L. Wang, C. Feng, et al., A superb mechanical behavior of newly developed lightweight and ductile Al0.5Ti2Nb1Zr1Wx refractory high entropy alloy via nano-precipitates and dislocations induced-deformation, Mater. Des. 222 (2022) 111034.
- [30] E.B. Tadmor, N. Bernstein, A first-principles measure for the twinnability of FCC metals, J. Mech. Phys. Solids 52 (11) (2004) 2507–2519.
- [31] G. Dirras, H. Couque, L. Lilensten, et al., Mechanical behavior and microstructure of Ti20Hf20Zr20Ta20Nb20 high-entropy alloy loaded under quasi-static and dynamic compression conditions, Mater. Charact. 111 (2016) 106–113.
- [32] Y. Long, X. Liang, K. Su, et al., A fine-grained NbMoTaWVCr refractory highentropy alloy with ultra-high strength: Microstructural evolution and mechanical properties, J. Alloy. Compd. 780 (2019) 607–617.
- [33] S.Y. Chen, X. Yang, K.A. Dahmen, et al., Microstructures and crackling noise of AlxNbTiMoV high entropy alloys, Entropy 16 (2) (2014) 870–884.
- [34] M.A. Khan, M. Hamza, J. Brechtl, et al., Development and characterization of a low-density TiNbZrAlTa refractory high entropy alloy with enhanced compressive strength and plasticity, Mater Charact 205 (2023) 113301.
- [35] D.F. Rojas, H. Li, O.K. Orhan, et al., Mechanical and microstructural properties of a CoCrFe0. 75NiMo0. 3Nb0. 125 high-entropy alloy additively manufactured via cold-spray, J. Alloy. Compd. 893 (2022) 162309.
- [36] M.A. Khan, Y. Wang, M. Hamza, et al., Precipitation behaviour in an Al-Zn-Mg-Cu alloy subjected to high strain rate compression tests, Mater Charact 180 (2021) 111398.
- [37] J. Málek, J. Zýka, F. Lukáč, et al., The effect of processing route on properties of HfNbTaTiZr high entropy alloy, Materials 12 (23) (2019) 4022.
- [38] M. J. Donachie, Titanium: a technical guide: ASM international, 2000.
- [39] J.G. Kaufman, Introduction to aluminum alloys and tempers, ASM International, 2000.
- [40] M. Li, Quantized dislocations, J. Phys. Condens. Matter 31 (8) (2019) 083001.
- [41] K. Ren, H. Liu, R. Ma, et al., Dynamic compression behavior of TiZrNbV refractory high-entropy alloys upon ultrahigh strain rate loading, J. Mater. Sci. Technol. 161 (2023) 201–219.
- [42] T. Zhang, Z. Jiao, Z. Wang, J. Qiao, Dynamic deformation behaviors and constitutive relations of an AlCoCr1. 5Fe1. 5NiTi0. 5 high-entropy alloy, Scr. Mater. 136 (2017) 15–19.

- [43] J.T.M. De Hosson, A. Roos, E. Metselaar, Temperature rise due to fast-moving dislocations, Philos. Mag. A 81 (5) (2001) 1099–1120.
- [44] A. Huang, S.J. Fensin, M.A. Meyers, Strain-rate effects and dynamic behavior of high entropy alloys, J. Mater. Res. Technol. 22 (2023) 307–347.
- [45] N. Kumar, Q. Ying, X. Nie, et al., High strain-rate compressive deformation behavior of the Al0. 1CrFeCoNi high entropy alloy, Mater. Des. 86 (2015) 598–602.
- [46] X.-F. Liu, Z.-L. Tian, X.-F. Zhang, et al., "Self-sharpening" tungsten high-entropy alloy, Acta Mater. 186 (2020) 257–266.
- [47] S. Gangireddy, B. Gwalani, K. Liu, et al., Microstructures with extraordinary dynamic work hardening and strain rate sensitivity in Alo. 3CoCrFeNi high entropy alloy, Mater. Sci. Eng. A 734 (2018) 42–50.
- [48] L. Wang, J. Qiao, S. Ma, et al., Mechanical response and deformation behavior of Alo. 6CoCrFeNi high-entropy alloys upon dynamic loading, Mater. Sci. Eng. A 727 (2018) 208–213.
- [49] B. Wang, C. Wang, B. Liu, X. Zhang, Dynamic mechanical properties and microstructure of an (Alo. 5CoCrFeNi) 0.95 Moo. 025Co. 025 high entropy alloy, Entropy 21 (12) (2019) 1154.
- [50] Y. Chen, Y. Li, X. Cheng, et al., The microstructure and mechanical properties of refractory high-entropy alloys with high plasticity, Materials 11 (2) (2018) 208.
- [51] H. Song, D.G. Kim, D.W. Kim, et al., Effects of strain rate on room-and cryogenic-temperature compressive properties in metastable V10Cr10Fe45Co35 high-entropy alloy, Sci. Rep. 9 (1) (2019) 6163.
- [52] C. Li, Y. Xue, M. Hua, et al., Microstructure and mechanical properties of AlxSiO. 2CrFeCoNiCu1 – x high-entropy alloys, Mater. Des. 90 (2016) 601–609.
- [53] W. Jiang, X. Gao, Y. Guo, et al., Dynamic impact behavior and deformation mechanisms of Cr26Mn20Fe20Co20Ni14 high-entropy alloy, Mater. Sci. Eng. A 824 (2021) 141858.
- [54] N. Li, W. Chen, J. He, et al., Dynamic deformation behavior and microstructure evolution of CoCrNiMox medium entropy alloys, Mater. Sci. Eng. A 827 (2021) 142048.
- [55] X. Zhong, Q. Zhang, J. Xie, et al., Mechanical properties and microstructure of the Alo. 3CoCrFeNiTiO. 3 high entropy alloy under dynamic compression, Mater. Sci. Eng. A 812 (2021) 141147.
- [56] Z. Li, S. Zhao, S.M. Alotaibi, et al., Adiabatic shear localization in the CrMnFeCoNi high-entropy alloy, Acta Mater. 151 (2018) 424–431.

- [57] C. Zener, J.H. Hollomon, Effect of strain rate upon plastic flow of steel, J. Appl. Phys. 15 (1) (1944) 22–32.
- [58] M.A. Afifi, Y.C. Wang, T.G. Langdon, Effect of dynamic plastic deformation on the microstructure and mechanical properties of an Al–Zn–Mg alloy, Mater. Sci. Eng. A 784 (2020) 139287.
- [59] W. Guo, J. Liu, J. Yang, S. Li, Effect of initial temperature on dynamic recrystallization of tungsten and matrix within adiabatic shear band of tungsten heavy alloy, Mater. Sci. Eng. A 528 (19–20) (2011) 6248–6252.
- [60] H. Saka, T. Imura, Direct measurement of mobility of edge and screw dislocations in 3% silicon-iron by high voltage transmission electron microscopy, J. Phys. Soc. Jpn. 32 (3) (1972) 702–716.
- [61] A. Seeger, C. Wüthrich, Dislocation relaxation processes in body-centred cubic metals, Il Nuovo Cimento B 1971–1996 (33) (1976) 38–75.
- [62] A.G. Odeshi, M.N. Bassim, S. Al-Ameeri, Effect of heat treatment on adiabatic shear bands in a high-strength low alloy steel, Mater. Sci. Eng. A 419 (1) (2006) 69–75.
- [63] T. Bhattacharjee, I. Wani, S. Sheikh, et al., Simultaneous strength-ductility enhancement of a nano-lamellar AlCoCrFeNi2. 1 eutectic high entropy alloy by cryo-rolling and annealing, Sci. Rep. 8 (1) (2018) 3276.
- [64] S.G. Kim, Y.B. Park, Grain boundary segregation, solute drag and abnormal grain growth, Acta Mater. 56 (15) (2008) 3739–3753.
- [65] P. Lejček, S. Hofmann, Thermodynamics of grain boundary segregation and applications to anisotropy, compensation effect and prediction, Crit. Rev. Solid State Mater. Sci. 33 (2) (2008) 133–163.
- [66] D. McLean, A. Maradudin, Grain boundaries in metals, American Institute of Physics, 1958.
- [67] P. Lejček, S. Hofmann, M. Všianská, M. Šob, Entropy matters in grain boundary segregation, Acta Mater. 206 (2021) 116597.
- [68] A.H. Cottrell, M. Jaswon, Distribution of solute atoms round a slow dislocation, Proc. R. Soc. London. Series A. Math. Phys. Sci. 199 (1056) (1949) 104–114.
- [69] D. Blavette, E. Cadel, A. Fraczkiewicz, A. Menand, Three-dimensional atomic-scale imaging of impurity segregation to line defects, Science 286 (5448) (1999) 2317–2319.
- [70] T. Hu, K. Ma, T. Topping, et al., Precipitation phenomena in an ultrafine-grained Al alloy, Acta Mater. 61 (6) (2013) 2163–2178.